



HAL
open science

Optimizing BOLD sensitivity in the 7T Human Connectome Project resting-state fMRI protocol using plug-and-play parallel transmission

Vincent Gras, Benedikt A. Poser, Xiaoping Wu, Raphaël Tomi-Tricot, Nicolas Boulant

► To cite this version:

Vincent Gras, Benedikt A. Poser, Xiaoping Wu, Raphaël Tomi-Tricot, Nicolas Boulant. Optimizing BOLD sensitivity in the 7T Human Connectome Project resting-state fMRI protocol using plug-and-play parallel transmission. *NeuroImage*, 2019, 195, pp.1 - 10. 10.1016/j.neuroimage.2019.03.040 . hal-03484588

HAL Id: hal-03484588

<https://hal.science/hal-03484588v1>

Submitted on 20 Dec 2021

HAL is a multi-disciplinary open access archive for the deposit and dissemination of scientific research documents, whether they are published or not. The documents may come from teaching and research institutions in France or abroad, or from public or private research centers.

L'archive ouverte pluridisciplinaire **HAL**, est destinée au dépôt et à la diffusion de documents scientifiques de niveau recherche, publiés ou non, émanant des établissements d'enseignement et de recherche français ou étrangers, des laboratoires publics ou privés.



Distributed under a Creative Commons Attribution - NonCommercial 4.0 International License

Optimizing BOLD sensitivity in the 7 T Human Connectome Project resting-state fMRI protocol using plug-and-play parallel transmission

Vincent Gras^a, Benedikt A Poser^b, Xiaoping Wu^c, Raphal Tomi-Tricot^b,
Nicolas Boulant^{a,*}

^a*NeuroSpin, CEA, University of Paris-Saclay, Gif-sur-Yvette, France*

^b*Department of Cognitive Neuroscience, Faculty of Psychology and Neuroscience,
Maastricht University, Maastricht, The Netherlands*

^c*Center for Magnetic Resonance Research, University of Minnesota, Minneapolis,
Minnesota, USA*

Abstract

The Human Connectome Project (HCP) has a 7 T component that aims to study the human brain's organization and function with high spatial and temporal resolution fMRI and diffusion-weighted acquisitions. For whole brain applications at 7 T, a major weakness however remains the heterogeneity of the radiofrequency transmission field (B_1^+), which prevents from achieving an optimal signal and contrast homogeneously throughout the brain. In this work, we use parallel transmission (pTX) Universal Pulses (UP) to improve the flip angle homogeneity and demonstrate their application to highly accelerated multi-band EPI (MB5 and GRAPPA2, as prescribed in the 7 T HCP protocol) sequence, but also to acquire at 7 T B_1^+ -artefact-free T_1 - and T_2 -weighted anatomical scans used in the pre-processing pipeline of the HCP

*To whom correspondence should be addressed. Postal address: Commissariat lnergie atomique et aux nergies alternatives Centre de Saclay — Batiment 145 P.C. 156 — 91191 Gif-sur-Yvette Cedex, FRANCE. E-mail: nicolas.boulant@cea.fr

protocol. As compared to typical implementations of pTX, the proposed solution is fully operator-independent and allows "plug and play" exploitation of the benefits offered by multi-channel transmission. Validation in five healthy adults shows that the proposed technique achieves a flip angle homogeneity comparable to that of a clinical 3 T system. Compared to standard single-channel transmission, the use of UPs at 7 T yielded up to a two-fold increase of the temporal signal-to-noise ratio in the temporal lobes as well as improved detection of functional connectivity in the brain regions most strongly affected by B_1^+ inhomogeneity.

Keywords: parallel transmission, Human Connectome Project, calibration, universal pulse, RF shimming, ultra-high field, multi-band EPI

1. Introduction

In functional magnetic resonance imaging (fMRI), there is a growing interest in performing neuro-scientific studies at ultra-high field (UHF) to benefit from the supra-linear increase in the blood oxygenation level dependent (BOLD) signal change with the static magnetic field strength (B_0) (Yacoub et al., 2001). Following this trend, e.g. the original young adult Human Connectome Project (HCP) contains a 7 T component that targets functional and diffusion MRI with high spatiotemporal resolutions (Uğurbil et al., 2013, Van Essen et al., 2013) to study the brain's organization and some of its functions. The 7 T HCP resting state fMRI (RS-fMRI) protocol comprises a ten-fold accelerated ($\times 5$ simultaneous multi-slice and $\times 2$ in-plane acceleration) multi-band echo-planar imaging (MB-EPI, a.k.a. SMS-EPI) acquisition which allows sampling the BOLD signal at 1.6 mm spatial and 1 s temporal

14 resolution.

15 A major challenge of 7 T MRI with large volume coverage is the het-
16 erogeneity of the radiofrequency (RF) transmission field (B_1^+) which, if not
17 corrected, would result in nonuniform flip angles and tissue contrast across
18 the whole brain. The RF nonuniformity is due to standing wave effects that
19 become problematic in the head at B_0 of 7 T and up, where the RF wave-
20 length becomes comparable to the head size and falls below 13 cm. The
21 consequence of the resulting flip-angle variation in 7 T (RS-fMRI) scans such
22 as the ones used in the 7 T HCP study is a reduced performance in the de-
23 tection of BOLD signal mostly in the inferior and temporal brain regions.
24 Similarly affected at 7 T are the magnetization prepared rapid gradient echo
25 (MPRAGE) (Mugler and Brookeman, 1990) and 3D variable flip angle turbo
26 spin echo (3D-VFA-TSE, a.k.a. SPACE (Mugler et al., 2000)) acquisitions
27 which are part of the minimal pre-processing pipeline of the HCP protocol
28 (Glasser et al., 2013). The inherent limits of these anatomical scans yet can
29 be compensated by providing 3 T images to complement the 7 T fMRI scans
30 (Glasser et al., 2013) but it remains desirable to be able to conduct the entire
31 set of acquisitions at 7 T.

32 In order to mitigate the problem of flip-angle inhomogeneity at UHF, the
33 7 T HCP has adopted a practical approach, which is to place dielectric pads
34 (filled with calcium titanate) around the head near the regions most strongly
35 affected. The high dielectric constant of the padding material ($\epsilon_r = 100$
36 or higher) notably affects the properties of the environment 'seen' by the
37 RF waves and, if placed adequately, steers them so as to locally enhance
38 the RF field (Webb, 2011). While effective locally, it appears extremely

39 challenging to achieve homogeneous RF fields over extended regions with the
40 use of dielectric pads alone.

41 Parallel RF transmission (pTX) technology (Katscher et al., 2003, Zhu,
42 2004) is one more elaborate approach to improve flip-angle uniformity, and
43 use of this still not wide-spread technology has recently been proposed for
44 whole-brain RS-fMRI acquisition at the same spatiotemporal resolutions as
45 in the 7 T HCP (Wu et al., 2019). Specifically, in this work, the MB-EPI se-
46 quence (Moeller et al., 2010, Setsompop et al., 2012, Vu et al., 2017) used in
47 HCP was modified to enable slice-specific RF shimming. In doing so, the co-
48 efficient of variation (CV), i.e., standard deviation (std)/mean) of the whole
49 brain flip-angle distribution, was $\sim 15\%$ for pTx (with eight independent
50 transmit channels) versus $\sim 24\%$ for conventional single channel transmis-
51 sion (sTX) , and $\sim 20\%$ if 3D whole-head RF shimming was performed (Gras
52 et al., 2017a, Krishnamurthy et al., 2019). This proved useful in enhancing
53 the temporal SNR especially in the regions adversely affected by voids in B_1^+ .
54 Other studies have also shown the potential of pTX technology to recover
55 optimal signal and contrast across the whole brain at 7 T in MPRAGE (Cloos
56 et al., 2012a), diffusion (Wu et al., 2018) as well as 3D TSE (Eggenschwiler
57 et al., 2014, Massire et al., 2015, Beqiri et al., 2018, Gras et al., 2018) acqui-
58 sitions.

59 However one drawback of those conventional pTX approaches is that the
60 optimized pTX excitations or refocusing were obtained by subject-specific nu-
61 merical optimization, performed 'online' (i.e., while the subject was waiting
62 in the scanner), based on subject- and session-specific B_1^+ maps that first had
63 to be acquired in the same session. In practice, this requires an additional

64 B_1^+ calibration scan whose duration amounts to at least 20s per transmit
65 channel for optimized B_1^+ mapping sequences, and the subsequent numerical
66 optimization of the pTX excitation which can also take up to several minutes.

67 The concept of Universal Pulse design (Gras et al., 2017b) offers a so-
68 lution for entirely removing the need for subject- or session-specific field
69 mapping and subsequent on-line optimization of the RF pulses. The benefits
70 of pTX are instead utilized in a fully automated or "plug-and-play" manner,
71 offering more flexibility and reactivity for the operator during the exam. In
72 contrast, full automation starting from subject-based acquired B_1^+ maps and
73 comprising on-line RF pulse tailoring in principle is possible but to date is
74 not available, and would still require extensive developments. Plug-and-play
75 pTX here is done by pre-calculating RF pulses that were optimized on a series
76 of B_1^+ and B_0 offset maps obtained from a representative sample of the adult
77 population. The RF pulse optimization thus takes place separately from the
78 scan session, and consists in minimizing an objective function that maximizes
79 the average performance of the pTX excitation across the database of field
80 maps (Gras et al., 2017a). The result of this procedure is universally valid
81 pulses, hence the term Universal Pulses (UP).

82 To better cope with inter-subject variability of the B_1^+ profile, UPs are
83 often designed by considering a broader class of pTX excitation modes than
84 RF shimming, namely *dynamic* RF shimming (Padormo et al., 2016). Here,
85 the capabilities of pTX are more fully exploited in that dynamic RF shim-
86 ming pulses take advantage of the transmit-sense (Katscher et al., 2003)
87 concept to homogenize the flip angle distribution. One potential weakness
88 with such types of excitation yet is the possible increase in the excitation du-

89 ration as compared to standard RF shimming, with impact on the response
90 of off-resonant spins but which can be taken into account in the pulse opti-
91 mization (Grissom et al., 2006). The most prominent examples for this are
92 2D spokes excitation (Saekho et al., 2006, Setsompop et al., 2008) and 3D
93 k_T -points (Cloos et al., 2012b) which apply small "gradient blips" in between
94 a series of selective or non-selective pulses, so as to spatially modulate the
95 flip angle phase of each subpulse and yield an overall more homogeneous flip
96 angle distribution within a slice or across a volume. Importantly, as shown
97 by Tse and colleagues in recent work at 9.4 T (Tse et al., 2016), the 2D
98 multi-spoke dynamic RF shimming technique can be extended to generate
99 pTX multi-band RF pulses that simultaneously excite multiple slices.

100 In this work, we report on the design of multi-band Universal Pulses to
101 conduct HCP-style RS-fMRI studies at 7 T. As in the original 7 T HCP, the
102 RS-fMRI was acquired using a 2D SMS sequence with factor-5 slice accelera-
103 tion. We also show that a complete shift towards 7 T acquisitions is possible,
104 with additional pTX-UP enabled T_1 - and T_2 -weighted anatomical scans that
105 can be incorporated in the preprocessing pipeline. The excitation pulse of the
106 MB-EPI sequence was replaced by bipolar two-spoke (MB-5) UPs, the non-
107 selective square pulses of the SPACE acquisition by a scalable (Eggenschwiler
108 et al., 2014, Gras et al., 2018) 9- k_T UP, the adiabatic inversion preparation
109 pulse of the MPRAGE sequence by a 9- k_T inversion UP, and the small FA
110 square pulse of the FLASH readout module of the MPRAGE sequence by a 7-
111 k_T UP. This pTX-UP implementation of the RS-fMRI protocol is compared
112 experimentally on five healthy adults with the same protocol played with
113 standard pulses and single channel transmission (sTX), without and with

114 dielectric pads. Using retrospective flip angle simulations based on measured
115 subject-specific B_1^+ maps, the benefit of the UP integration into the RS-fMRI
116 protocol in terms of signal homogeneity is compared with subject and slice
117 specific RF shimming strategies. Temporal SNR (tSNR) is quantified based
118 on the measured EPI time-series of each volunteer. A seed-based analysis
119 of the default mode network (DMN) is also reported to evaluate the gain in
120 terms of functional connectivity estimation.

121 **2. Material and Methods**

122 All experiments were performed on a 7T Siemens Magnetom MRI sys-
123 tem (Siemens Healthineers, Erlangen, Germany, software baseline VB17A
124 and step 2.3 pTX) equipped with an eight-channel pTX system (1kW per
125 channel), and SC72 body gradient coil (nominal slew rate 200 mT/m/ms and
126 40 mT/m maximum amplitude). The vendor-provided head-coils were used:
127 8Tx-32Rx for pTX acquisitions, 1Tx-32Rx for the sTx reference experiments
128 (both from Nova Medical, Wilmington, MA, USA). The implementation of
129 the HCP resting-state fMRI protocol used custom MB-EPI, MPRAGE and
130 SPACE sequences to enable pTX and UPs integration. Measurements were
131 performed on 5 healthy adult subjects (2 women) and were divided for each
132 one of them into three one-hour sessions, run on different days, to cover
133 the pTX and the sTX operation modes with and without dielectric padding.
134 The dielectric pads were based on a calcium titanate (CaTiO_3) suspension
135 (Webb, 2011) and were 0.5 cm thick and 10 cm long (square form). Two
136 such pads were placed against the subjects ears. For the acquisition in sTX,
137 the standard RF transmitter adjustment procedure provided by the scan-

138 ner’s manufacturer was used. In pTX, this calibration step was disabled
139 and the transmitter adjustment was specified by the UPs used in the respec-
140 tive sequences, as detailed below. Adherence to the SAR guidelines was en-
141 sured by real-time SAR supervision using a Virtual Observation Point (VOP)
142 model (Eichfelder and Gebhardt, 2011) of the SAR distribution in the head
143 that was implemented using home-made routines and electromagnetic simu-
144 lations provided by the coil vendor. After experimental phantom validation
145 on the scanner, the VOPs were augmented by safety factors to account for
146 RF coil modelling imperfections, inter-subject variability in the peak SAR
147 value (Garrec et al., 2016, Boulant et al., 2018) and uncertainties in the di-
148 rectional coupler measurements of the TX Array system (Gumbrecht, 2013),
149 resulting in a total safety factor of 2.3 (Boulant et al., 2018). The study
150 was approved by the local ethics committee and all volunteers gave written
151 informed consent.

152 *2.1. MRI protocol*

153 The MRI acquisition consisted of a 30 min resting-state (RS) fMRI proto-
154 col, followed by T_1 - and T_2 -weighted anatomical scans using the MPRAGE
155 and the SPACE sequences, respectively. An interferometric turbo-FLASH
156 B_1^+ mapping protocol (5 mm isotropic resolution, repetition time [TR] = 20 s,
157 acquisition time [TA] = 4 min 40 s) (Fautz et al., 2008, Brunner and Pruess-
158 mann, 2009) and multiple gradient recalled echo (GRE) protocol (2.5 mm
159 isotropic resolution, TR = 8.4 ms, 3 echoes, echo times [TE] = 2.7, 4.2, 6 ms,
160 TA = 30 s) were also added in order to quantitatively assess the B_1^+ and ΔB_0
161 distributions for each subject and each acquisition mode.

162 The RS-fMRI part used a 15 min fat-suppressed MB-EPI acquisition ap-

163 plied twice, with the in-plane phase encoding direction being flipped during
164 the second run (AP followed by PA). Subjects were instructed to keep their
165 eyes open and focus on a red fixation cross on a black screen. EPI acquisition
166 parameters were : 90 axial slices of 1.6 mm thickness with no gap, standard
167 sinc excitation (time-bandwidth product = 3.2, Hanning window apodiza-
168 tion), nominal flip angle = 45° , TR = 1 s, voxel size = $(1.6 \text{ mm})^3$, in plane field
169 of view (FOV) = $(208 \times 208) \text{ mm}^2$, multi-band slice acceleration factor = 5
170 with blipped-CAIPIRINHA FOV/3 inter-slice shift, in-plane GRAPPA accel-
171 eration factor = 2 with 52 autocalibration lines (ACS) acquired separately
172 using the fast low angle excitation echo-planar technique (FLEET) (Poli-
173 meni et al., 2016), partial Fourier acquisition = 7/8, readout bandwidth =
174 1832 Hz/pixel, fat saturation with nominal flip angle = 80° . Online image
175 reconstruction was performed with the implementation of the MGH blipped-
176 CAIPI MB-EPI C2P (www.nmr.mgh.harvard.edu/software/c2p/sms), which
177 uses sequential application of Slice-GRAPPA (Setsompop et al., 2012) with
178 leak-block (Cauley et al., 2014) and GRAPPA (Griswold et al., 2002).

179 The T_1 - and T_2 -weighted acquisitions were in sagittal orientation, isotropic
180 resolution of 0.8 mm, FOV = $(256 \times 224 \times 208) \text{ mm}^3$ (read, phase and par-
181 tition axes) and a GRAPPA acceleration factor of 2 in the phase encode di-
182 rection. Other parameters were: TR = 2.6/3.0 s, MPRAGE inversion time =
183 1.1 s, echo spacing (ES) = 10.2/8.6 ms, readout bandwidth = 240/370 Hz/pixel,
184 flip angle = 4° /Mugler's approach (Mugler, 2014, Mugler et al., 2000) respec-
185 tively for the MPRAGE and SPACE acquisitions.

186 *2.2. Design of parallel transmission Universal Pulses*

187 Dynamic RF shimming with spoke (slice-selective) and k_T -point (non-
 188 -selective) pulses use a simple and low-dimensional parameterization of the
 189 RF and gradient waveforms. It consists of i) the different RF shimming
 190 weights, defined by the time integral of the RF shim sub-pulses, and ii) the
 191 transmit k-space (Cloos et al., 2012b) displacement vectors, i.e. the time
 192 integral of the interleaved magnetic field gradient blips along the three axes.
 193 In this framework, efficient non-linear constrained optimization algorithms
 194 can be applied to attempt finding the best possible dynamic RF-shimming
 195 solution (Hoyos-Idrobo et al., 2014).

196 The UPs used for the MB-EPI, the MPRAGE and the SPACE acqui-
 197 sitions in pTX were designed offline on a database \mathcal{B} of measured subject-
 198 based B_1^+ and ΔB_0 maps of size $N_{\mathcal{B}} = 10$ (5 female), acquired in a sepa-
 199 rate study (Gras et al., 2017a). The UP design consisted in evaluating the
 200 subject-specific objective $\epsilon_{\text{tailored}}$ (typically a measure of the mean deviation
 201 of the flip angle distribution across the region of interest) on every subject of
 202 the database and computing the mean objective across this database. The
 203 UP-objective ϵ_{UP} may thus be written as:

$$\epsilon_{\text{UP}}(p) = \frac{1}{N_{\mathcal{B}}} \sum_{j \in \mathcal{B}} \epsilon_{\text{tailored}}(\mathcal{S}_j, p), \quad (1)$$

204 where p denotes the dynamic RF shimming parameterization to be optimized,
 205 and $\epsilon_{\text{tailored}}(\mathcal{S}_j, p)$, the evaluation of the subject-based objective on subject \mathcal{S}_j
 206 of the database for the parameterization p . Hence, without any additional
 207 difficulty, hardware (RF power and gradient slew rate limits) and safety
 208 (SAR) constraints can be enforced explicitly for the UP design following ex-
 209 actly the same methodology used for a subject-tailored pulse design. This

210 was implemented using the active-set non-linear constrained optimization al-
 211 gorithm (Hoyos-Idrobo et al., 2014), available in the optimization toolbox of
 212 MATLAB (R2016b, the Mathworks, Natick, MA). The hardware constraints
 213 were i) the peak RF amplitude limit (170 V per TX channel at the coil plug),
 214 ii) the average RF power limit per TX channel (3 W), iii) the total average
 215 RF power limit (16 W) and iv) the maximum slew rate of the magnetic field
 216 gradient coils (200 mT/m/ms). The SAR thresholds were expressed in terms
 217 of global and local SAR limits of 3.2 W/kg and 10 W/kg respectively (Inter-
 218 national Electrotechnical Commission, 2015).

219 For the design of the non-selective UPs (SPACE and MPRAGE sequences),
 220 the subject-tailored objective was defined as the normalized root mean square
 221 (NRMS) deviation of the flip angle distribution $\alpha(r)$ from the target flip angle
 222 α_T , calculated across the brain (region \mathcal{R}), i.e.:

$$\epsilon_{\text{tailored,3D}} = \frac{1}{|\alpha_T|} \left(\frac{1}{|\mathcal{R}|} \sum_{r \in \mathcal{R}} (\alpha(r) - \alpha_T)^2 \right)^{\frac{1}{2}}, \quad (2)$$

223 where $|\mathcal{R}|$ and r denote the number of brain voxels of the B_1^+ map and
 224 the spatial coordinates, respectively. For the design of the slice-selective
 225 UPs (MB-EPI sequence), the objective was formulated as a weighted NRMS
 226 deviation from the target flip angle across the brain with the slice-dependent
 227 weighting function:

$$w(r) = \exp \left(-d_0^{-1} \max \left(0, d(r, \mathcal{P}) - \frac{\theta}{2} \right) \right) \quad (3)$$

228 where \mathcal{P} denotes the median plane of the considered slice, $d(r, \mathcal{P})$ the Eu-
 229 clidean distance from r to \mathcal{P} , θ the slice thickness, and $d_0 = 1$ cm. The

230 objective in this case for a single slice thus is given by the equation:

$$\epsilon_{\text{tailored,2D}} = \left(\frac{1}{\sum_{r \in \mathcal{R}} w(r)} \sum_{r \in \mathcal{R}} w(r) (\alpha(r) - \alpha_T)^2 \right)^{\frac{1}{2}}. \quad (4)$$

231 We note here that taking $d_0 = 0^+$ leads to the weighting function $w = 1$ for
 232 $r \in \mathcal{P}$, which is the conventional way of designing slice-specific spokes pulses.
 233 Taking into account all voxels in \mathcal{R} , and letting the flip angle deviation have
 234 an (exponentially) decreasing weight as the distance from the slice of interest,
 235 promotes robustness of the pulse against variations in the slice positions and
 236 small tilts. Likewise, taking $d_0 = \infty$, leads to $w = 1$ everywhere and the
 237 2D objective converges to the 3D objective in that case. The choice of a
 238 1 cm soft threshold was found to offer a good compromise between excitation
 239 performance and robustness.

240 In equations 2 and 4, for all but the inversion pulse, the flip angle distri-
 241 bution $\alpha(r)$ was computed using the small tip angle approximation (Pauly
 242 et al., 1989a). This approximation provides a linear relationship between
 243 the RF weights and the flip angle (Boulant and Hoult, 2012) which is valid
 244 for up to moderate target flip angles or for symmetric pulses (Pauly et al.,
 245 1989b, Eggenschwiler et al., 2014, Gras et al., 2018). For the inversion pulse,
 246 this approximation being not valid, $\alpha(r)$ was obtained by numerical integra-
 247 tion of Bloch’s equations (Bloch integration). For the computation of $\alpha(r)$,
 248 relaxation effects during the pulse were neglected.

249 For the design of the MB-EPI UPs, coherent summation of the slice-
 250 specific RF pulses within each multiband slice group was assumed for sim-
 251 plicity to ensure that peak RF amplitude of the multiband waveforms of any
 252 slice group did not exceed the hardware peak power limit. This has a sim-

253 ple and tractable implementation as it involves only a reasonable number of
254 constraints per multiband slice group (the product of the number of transmit
255 channels by the number of spokes). For this particular scenario (8 transmit
256 channels, two spokes and MB-5), the subsequent optimization of the global
257 (consistent across all transmit channels and spokes) RF phase offsets between
258 the different slices of the same multiband slice group (Wong, 2012) returned
259 a reduction of peak amplitude of 20%.

260 Owing to the smooth variation of the B_1^+ field and the weighting func-
261 tion in the 2D objective above, RF coefficients and spokes-placement in k-
262 space (Dupas et al., 2015) were optimized for every other slice only (45 slices
263 among 90) and the same parametrization was attributed to the adjacent
264 slice (Wu et al., 2013, Tse et al., 2016). To comply with the multiband accel-
265 eration (here of 5), the spoke placement optimization was done concurrently
266 for all slices of a multiband group (the set of slices excited simultaneously).
267 Finally, the bipolar two-spoke pulses were designed with a subpulse duration
268 of 2180 μs and a total pulse duration of 4800 μs (excluding the slice selec-
269 tion rewinder). Prior to designing the bipolar spokes, the gradient delay
270 was characterized on phantom using sub- μs precision and compensated for
271 by manipulating the RF phase of the second spoke (Gras et al., 2017c).
272 As shown also elsewhere (Tse et al., 2016), characterizing and correcting
273 for this delay with such precision is a necessary ingredient for multi-bipolar
274 spoke applications away from the iso-center. Unipolar designs, where both
275 slice selection gradients share the same polarity, are inherently insensitive to
276 these imperfections but they have less spectral bandwidth due to a longer
277 duration and are more prone to peripheral nerve stimulations due to the

278 additional gradient lobe.

279 The pTX UP MPRAGE acquisition used k_T -point pulses (Cloos et al.,
280 2012b) for the 4° excitation and 180° inversion pulses, as described in ref. (Gras
281 et al., 2017a). The excitation used 4° flip angle (800 μs total duration with
282 7 gradient blips of 40 μs each) while the 180° inversion pulse lasted 4000 μs
283 (9 subpulses of 400 μs each). The sTX pulse implementation used a stan-
284 dard 700 μs -long square pulse for the 4° excitation and a standard 10 ms
285 hyperbolic-secant adiabatic pulse for inversion.

286 The pTX UP SPACE acquisition was based on a unique scalable (Eggen-
287 schwiler et al., 2014) k_T -point pulse (9 subpulses, total duration = 1100 μs),
288 consistently with the methodology proposed in ref. (Gras et al., 2018). The
289 leading excitation pulse was implemented using the same k_T -point pulse, but
290 scaled to produce a 90° flip angle and with 90° phase offset to satisfy the
291 Carr-Purcell-Meiboom-Gill (CPMG) condition. Scalability of the refocusing
292 pulses, was enforced by exploiting symmetries and applying a dedicated op-
293 timization routine (Gras et al., 2018). This allowed using a unique k_T -point
294 pulse to implement the entire array of non-selective pulses of the variable
295 flip angle TSE readout and the preceding 90° excitation. The sTX imple-
296 mentations of the SPACE acquisition used standard 500 μs - and 700 μs -long
297 square pulses for the 90° excitation and the variable flip angle TSE readout
298 respectively.

299 *2.3. Analysis of pulse performance and additional simulations*

300 The RF pulse performance was assessed post-hoc by performing voxel-
301 wise Bloch simulations using the B_1^+ and B_0 offset maps that were acquired
302 on each subject in addition to the (f)MRI scans. The CV of the flip angle

303 and the MR signal were calculated across the brain. The interest of analyzing
304 the signal homogeneity (as the ultimate measure of interest in practice) in
305 addition to the flip angle (the physical parameter that drives the RF pulse
306 optimization) is to take into account the non-linear dependence of MR signal
307 with the flip angle. The MR signal was computed for a representative pair
308 of T_1/T_2 values for brain white matter at 7 T, namely 1300/60 ms.

309 For the MB-EPI sequence, to provide a comparison of the proposed two-
310 spoke UP design with the volume (global) (Krishnamurthy et al., 2019) and
311 slice-specific RF shimming (Wu et al., 2019) (one-spoke pulses), additional
312 sets of simulations were performed in which the bipolar two-spoke design
313 was replaced with the (simpler) one-spoke design (pulse duration 4520 μs),
314 with otherwise identical design parameters as for the 2-spoke UPs): i) a
315 set of 45 slice-specific *universal* RF-shims using the database of B_1^+ and B_0
316 offset maps and the UP objective, ii) a set of 45 slice-specific and subject-
317 tailored (Wu et al., 2019) RF-shims per subject, and iii) a global ($d_0 \rightarrow \infty$)
318 subject-tailored RF-shim over the whole head, per subject.

319 The gain in robustness with respect to slice position and inclination pro-
320 vided by the weighted least-squares approach (see Equation 4) was also tested
321 through the following simulation. The 45-slice UP design for the MB-EPI
322 protocol was repeated with a weighted-least squares soft threshold d_0 (see
323 Equation 3) of 1 mm (instead of 10 mm). The coefficient of variation of the
324 flip angle (45 slices merged together) of both sets of pulses was then com-
325 puted for different values of slice position offsets (up to 20 mm) and slice
326 inclinations (rotation about the right-left axis of up to 20°).

327 *2.4. fMRI pre-processing and temporal SNR calculations*

328 The MB-EPI data were first motion-corrected using FSL McFLIRT (Jen-
329 inson et al., 2002). The two 900-volume series (with AP and PA phase encod-
330 ing directions) of each session were then distortion-corrected based on FSL
331 Topup (Andersson et al., 2003). The temporal SNR was then calculated for
332 each voxel, subject and session by taking the mean of the corresponding time-
333 series divided by its standard deviation, after linear de-trending and removal
334 of the first 10 volumes to reject the transient spin evolution towards steady-
335 state from the analysis. The tSNR maps were then registered to the Montreal
336 Neurological Imaging (MNI152) template by using the FSL FLIRT affine reg-
337 istration tool with 12 degrees of freedom (Jenkinson and Smith, 2001), aided
338 by the T_1 -weighted anatomical scan. This allowed computation of an average
339 tSNR map across subjects and generation of inflated cortical surface repre-
340 sentations by using PySurfer (<https://github.com/nipy/PySurfer>). In order
341 to provide a common ground and not bias the comparison of sTX versus
342 pTX, the same (pTX) T_1 -weighted scan was used for the registration.

343 *Analysis of the resting-state data*

344 After motion correction, distortion correction and registration as de-
345 scribed above, the time varying signals associated to each voxel were stan-
346 dardized to display a unit-variance, detrended and band-pass filtered (0.01-
347 0.1 Hz) (Goelman et al., 2017). The 6 motion parameters (3 for translation, 3
348 for rotation) of the time-series realignment procedure and physiological noise
349 related confounds were regressed out using CompCor (Behzadi et al., 2007).

350 Correlated BOLD fluctuations were identified using the seed-based ap-
351 proach, by selecting a voxel in the brain (seed) and calculating the correlation

352 between its associated signal and all other voxel time-series. For the present
353 analysis, the seed was a spherical volume of 8 mm in diameter located in the
354 posterior cingulate cortex (center coordinates: $[0, -50, 26]$ on the MNI152
355 template). For all voxels across the brain, the Pearson correlation coefficient
356 relative to this seed was then calculated and mapped onto inflated cortical
357 surfaces using nilearn (Abraham et al., 2014).

358 In the resting brain, The BOLD signal in the posterior cingulate cortex is
359 known to correlate with the one observed in the inferior parietal and medial
360 prefrontal cortices as well as the temporal cortex (Raichle et al., 2001, Vincent
361 et al., 2006), thus characterizing the so-called default mode network. The
362 aim of this analysis hence was to reproduce this finding on a subject-by-
363 subject basis and compare the correlation maps between acquisition modes.
364 The hypothesis here is that a better BOLD sensitivity translates into higher
365 correlations in this seed-based analysis of the DMN.

366 **3. Results**

367 *3.1. Comparison of image quality*

368 Figure 1 provides a comparison of the MB-EPI, MPRAGE and SPACE
369 acquisitions obtained in subjects 1 to 5 in pTX versus sTX. All sTX acqui-
370 sitions display signal losses in the temporal lobes, of which one coronal section
371 is shown in the figure. For the MB-EPI acquisition, this signal loss directly
372 affects BOLD sensitivity as the SNR and tSNR naturally scale with the MR
373 signal. The introduction of CaTiO_3 dielectric pads (second rows in a)-c))
374 somewhat reduces but does not eliminate the signal loss. For the SPACE
375 acquisition, which makes use of an optimized flip angle train to enable long

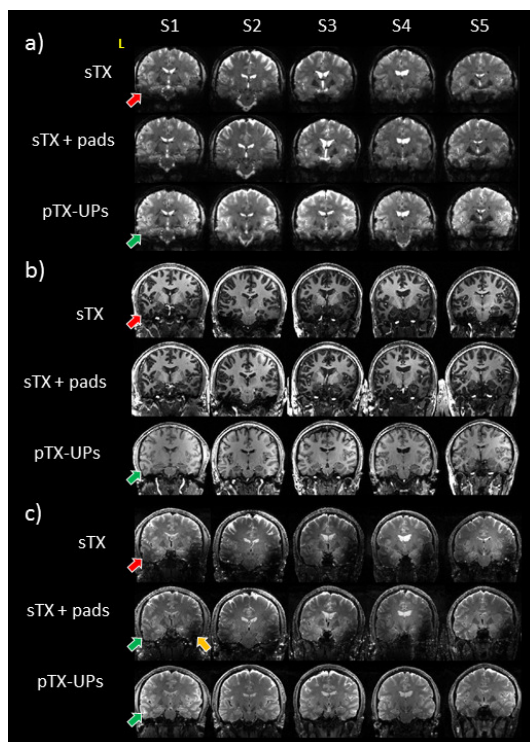


Figure 1: Image comparison comparisons for the different acquisition modes and sequences. EPI with MB=5 (a), b) MPRAGE and c) SPACE acquisitions obtained in subjects 1 to 5 in sTX (with and without dielectric padding) versus pTX are provided. For all subjects (S1 to S5), a marked signal loss is present in both sTX acquisitions (top and middle rows in a-c) in the temporal lobes (red arrows). For all subjects, such signal loss or contrast deterioration is absent in the pTX UP acquisitions (bottom row), as indicated by the green arrows. The dielectric pads (clearly visible in the MPRAGE and SPACE images) were able to compensate for the signal drop in all subjects, mostly in the left temporal lobe. As can be seen for instance in the SPACE acquisition of S1, the favorable influence of the dielectric pad however was clearly asymmetric as it was not able to restore a good contrast for the right temporal lobe (orange arrow).

376 TSE readouts, the flip angle heterogeneity severely degrades the signal and
377 the contrast in lower brain regions. As confirmed by the flip angle analysis
378 that follows, with pTX and universal k_T -point pulses, the flip angle error
379 is reduced to a level that is sufficient to obtain T_2 -weighted 3D images free
380 of B_1^+ artifacts. In the MPRAGE images, the improvement with UPs was
381 less pronounced because the preservation of the gray-white matter contrast
382 is mostly governed by the quality of the inversion preparation. In sTX, we
383 observed that the hyperbolic-secant adiabatic inversion pulse provided good
384 inversion efficiency over the whole brain, with the exception of a small portion
385 of the cerebellum or the temporal lobes in some subjects. The major image
386 imperfection that remains in the T_1 -weighted scans in sTX thus is a signal
387 drop in regions of low B_1^+ , more detrimental to SNR than image contrast.
388 As a general rule for MPRAGE, a smaller flip angle for the FLASH readout
389 leads to stronger contrast, but a weaker signal (Gras et al., 2016). As a re-
390 sult, undershot FLASH excitations in sTX results in a stronger gray-white
391 matter contrast, but a weaker SNR than observed in the pTX acquisitions.

392 *3.2. Assessment of RF pulse performance by simulation*

393 Figure 2 provides a comparison of the functional and anatomical images
394 that were obtained in one representative subject with the three acquisition
395 modes (pTX UPs, sTX and sTX with dielectric pads) evaluated in this study.
396 For the coronal plane that is displayed, the associated flip angle distribution
397 obtained retrospectively in simulation using the RF pulse definition and the
398 subject-specific B_1^+ and ΔB_0 maps is shown on the right side. The flip an-
399 gle profile in sTX displays flip angle values ranging from 30% to 110% of
400 the target value. Using pTX UP slice-specific two-spoke multi-band (for

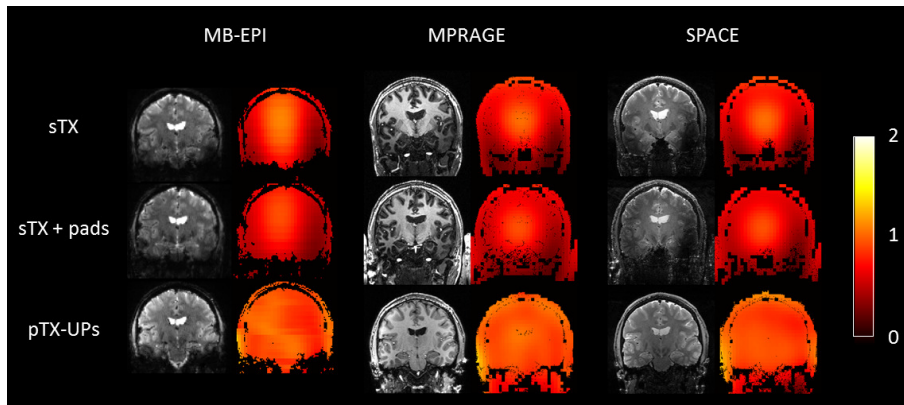


Figure 2: Coronal views for one representative subject of the MB-EPI, MPRAGE and SPACE images with corresponding simulated flip angle simulations. For every scan, the underlying flip angle distribution (obtained by retrospective simulation from the measured subject-specific B_1^+ and ΔB_0 distribution) is displayed in units of the nominal FA distribution. Even in the presence of dielectric pads, the sTX acquisition mode displays a strong flip angle heterogeneity, with values ranging from 30% up to 110% the nominal flip angle (respectively the 1%- and the 99%-quantiles of the flip angle distribution in the brain). This heterogeneity is largely removed in the pTX-UP acquisition mode.

401 MB-EPI) and volume-selective k_T -point pulses (for the MPRAGE inversion
 402 and FLASH pulses, and the SPACE excitation and refocusing pulses), much
 403 greater homogeneity of the excitation profiles is achieved.

404 The CV of the flip angle and the MR signal for $T_1/T_2 = 1300/60$ ms across
 405 the brain (i.e. the region of interest) with respect to the mean flip angle is
 406 reported in Table 1. These were computed for the 45° slice-selective pulses
 407 of the MB-EPI acquisition, the 4° non-selective pulse used in the MPRAGE
 408 sequence and the 90° excitation pulse used in the SPACE sequence. The sta-
 409 tistical significance of the flip angle and the signal heterogeneity reductions
 410 (pTX UP versus sTX) was also quantified using paired t-tests. For all se-

	pTX UPs			sTX		sTX+pads	
	FA	Signal	FA	Signal	FA	Signal	
MB-EPI	9-11	4-6	22-24	15-17 (2.10 ⁻⁵)	20-22	14-17 (8.10 ⁻⁵)	
MPRAGE	7-9	8-10	”	22-25 (7.10 ⁻⁶)	”	21-23 (3.10 ⁻⁶)	
SPACE	8-11	9-13	”	34-40 (3.10 ⁻⁵)	”	35-41 (4.10 ⁻⁶)	

Table 1: CV (in percent) of the flip angle (FA) and the MR signal (best case – worst case over 5 subjects) for the MB-EPI, the MPRAGE and the SPACE HCP-style protocols at 7 T. For the sTX acquisition mode, relative homogeneity is consistent for all sequence types given that pulses involved in those sequences do not use the dynamic RF shimming principle. The values displayed in parenthesis are p-values of statistical paired t-tests performed on the signal NRMS deviation between the pTX UP acquisitions and the sTX acquisitions.

411 quences, the CV of the MR signal was statistically significant ($p < 2 \times 10^{-5}$).
412 While the CV of the flip angle typically exceeds 25% in sTX, the UP approach
413 allows to restore an excitation uniformity at least as good as typically seen on
414 a clinical 3 T system (13%) with standard transmission hardware (Boulant
415 et al., 2008). Using pTX UPs, the CV of the MB-EPI signal ranged from
416 4% to 6% while it always exceeded 14% using sTX. For the 3D T₁-weighted
417 and T₂-weighted anatomical scans, the signal’s CV was below 13% in pTX
418 while it often exceeded 25% in sTX with and without dielectric padding. The
419 dielectric pads were helpful in compensating for the B₁⁺ drop in their vicinity
420 (the left and right temporal lobes) but, this had a minimal impact on the
421 CV, the latter criterion being a global performance measure.

422 The simulated flip angle homogeneity of the two-spoke versus the one-
423 spoke pulse designs for the pTX-enabled MB-EPI sequence is provided in

objective	#spokes	FA	Signal
universal	2	9-11	4-6
	1	12-16	5-8 ($p = 0.047$)
tailored s.s.	1	9-12	3-5 ($p = 0.8$)
tailored global	1	17-20	6-8 ($p = 0.005$)

Table 2: NRMS deviation (in percent) of the flip angle (FA) and the MR signal (best case – worst case over 5 subjects) for the slice-specific universal 2-spoke, tailored slice-specific (s.s.) and global RF shims, and universal 1-spoke pulse designs. Using universal 2-spoke pulses, the signal NRMS deviation is significantly lower than with universal 1-spoke pulses ($p = 0.047$). The same comparison with tailored 1-spoke pulses yet gives $p = 0.8$, i.e. no statistical evidence that the universal 2-spoke design outperforms the tailored 1-spoke design.

424 Table 2. The universal 2-spoke design (the one evaluated experimentally in
425 this work) is comparable in performance with the tailored 1-spoke design
426 ($p = 0.8$), applied in another study (Wu et al., 2019). This raises the ques-
427 tion whether a 1-spoke *universal* design, simpler than the 2-spoke universal
428 design, would be sufficient. In simulation, the 1-spoke UP design indeed
429 yields a significantly better signal CV than the sTX acquisition (5-8% versus
430 14-17%, $p = 0.047$), but a poorer homogeneity as compared to the two-spoke
431 universal or 1-spoke tailored design (3-6%). Hence for one subject, the flip
432 angle CV exceeds 16%, that is, a signal uniformity that is superior to that
433 observed on a clinical 3 T system (Boulant et al., 2008). The subject-specific
434 global RF shim on the other hand returned flip angle CVs of 17% up to 20%..

435 The robustness of the multiband UPs with respect to a shift in the slice
436 positions or an inclination of the slices is showed in Figure 3. As expected,

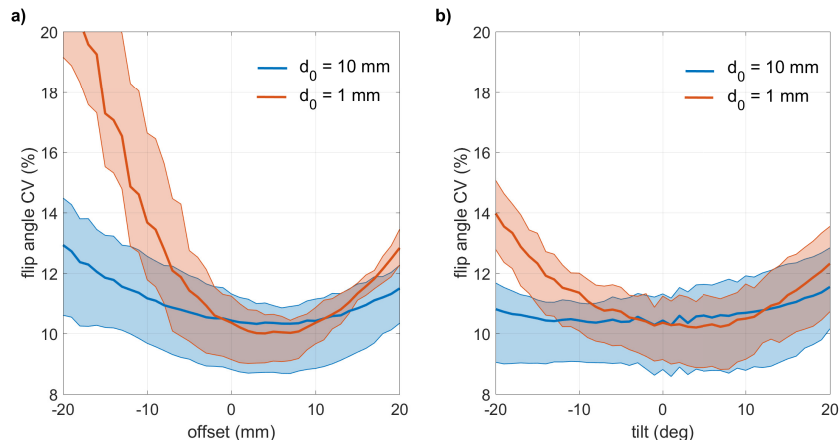


Figure 3: Simulation of the flip angle CV (45 slices pooled together) as a function of a) the slice shift and b) the slice inclination (about the right-left axis) for the universal pentaband pulses designed with a weighted least-squares parameter d_0 (see Equation 3) of 1 mm (red curve) and 1 cm (the proposed design parameter, blue curve). For each plot, the thick line and the two enclosing lines represent the mean, the minimum and the maximum of the CV across the five subjects.

437 the set of pulses obtained with the 1 cm soft-threshold perform better than
 438 the other with respect to a variation in the position or the inclination of
 439 the slice. Note that $d_0 = 1$ mm practically leads to no weighting since the
 440 spatial resolution of the B_1^+ maps is 5 mm. This result also indicates that
 441 the tolerance of the universal MB-EPI pulses designed in this study can be
 442 considered as high as 2 cm for the slice position offset and 20° for the slice
 443 inclination. Indeed, for both cases, the CV in flip angle does not exceed 13%.

444 3.3. Temporal SNR

445 Projections of the tSNR maps onto cortical surfaces for each subject are
 446 shown in Figure 4. In each subject, tSNR of the pTX UP scans exceeds that
 447 of the sTX acquisitions, without and with pads), which is consistent with

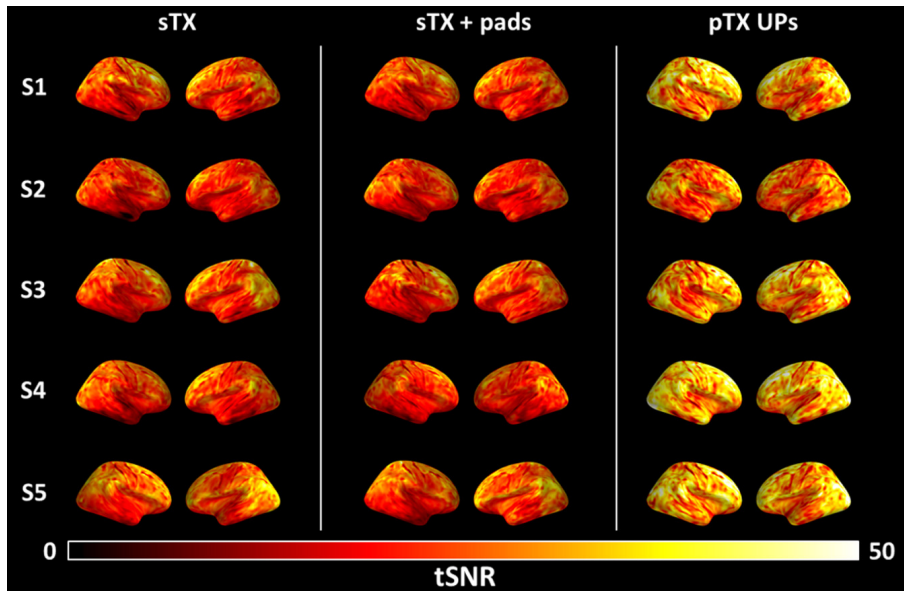


Figure 4: Cortical surface projection of the tSNR maps obtained for the left and right hemispheres for subjects 1 to 5 (top to bottom) and for the three different setups (left to right). Using pTX and UPs, a higher tSNR can be achieved over the cortex consistently throughout all subjects.

448 the flip angle simulations reported above. Additionally, a comparison of the
 449 average (across the five subjects after normalization to the MNI152 template)
 450 temporal SNR maps is displayed in Figure 5a. A marked tSNR gain with
 451 pTX can be seen, in particular in the temporal, occipital and parietal lobes,
 452 where the transmit efficiency of the RF coil in sTX is weaker. This is also
 453 demonstrated by the ratio maps (Figure 5b) which reveal tSNR gains of up
 454 to 100% between the pTX and the sTX acquisitions. On average across all
 455 subjects and over the whole brain, the tSNR gain using UPs amounted to
 456 25%.

457 In this study, we used a different, standard, (pre) processing pipeline (FSL

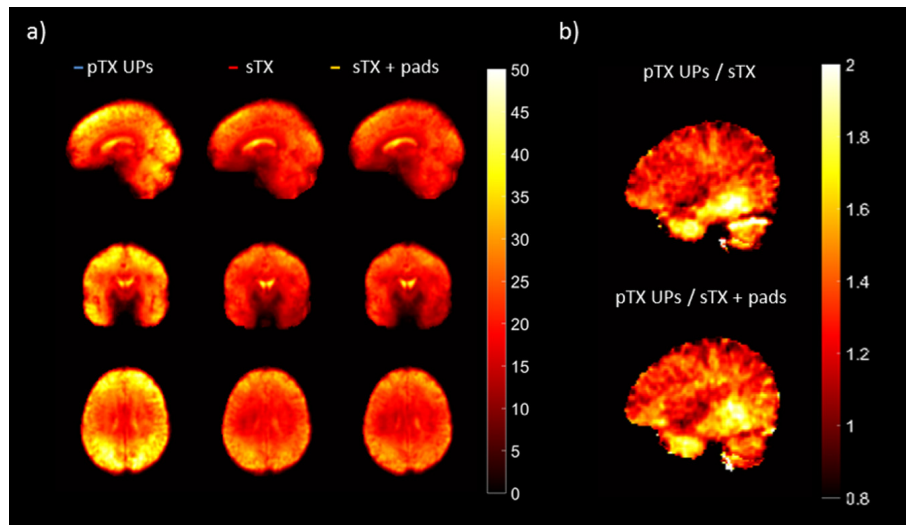


Figure 5: Average tSNR data. a) Three-plane view of the average (across all five subjects) tSNR map for the pTX UP (left column), in sTX (middle column) and sTX with dielectric pads (right column) acquisitions. Averaging was performed after normalization to the MNI152 standard space. b) tSNR ratio maps of pTX/sTX and pTX/sTX with pads shown for one sagittal slice through the right temporal lobe, showing a considerable tSNR enhancement in that region for the UP approach.

458 for realignment and distortion correction, nilearn for normalization and de-
459 noising) than the one defined in the HCP protocol (Van Essen et al., 2013),
460 and in which the T₂-weighted scan was not employed for registration and
461 segmentation. However, for the HCP data analysis framework, the contrast
462 uniformity enhancement enabled by UPs for the T₂-weighted acquisition (see
463 Figure 1) could be beneficial to improve the quality of the segmentation. In
464 this study, We found for instance that the registration to the MNI template
465 using FSL (with default processing parameters) was more robust if the pTX-
466 rather than the sTX-MPRAGE acquisition was selected as the input anatom-
467 ical image. We shall note however that a more thorough and expert use of
468 the software could have improved the robustness of the registration with the
469 sTX-MPRAGE acquisition.

470 *3.4. Resting-state analysis*

471 Figure 6 reports the seed-based analysis of the DMN performed on all
472 subjects and for all setups. Here, stronger time-correlations between the
473 posterior cingulate cortex and the temporal cortex can be seen in the data
474 acquired with pTX UPs. This observation is consistent with the reported
475 tSNR increase in the same regions. However, due to the small number of
476 subjects involved in this study, no statistical analysis of the increased time-
477 correlation was performed. It is also interesting to note a more pronounced
478 left-right symmetry in the pTX UP results, which conforms to the description
479 of the DMN as a symmetric network in the literature (Smith et al., 2009).

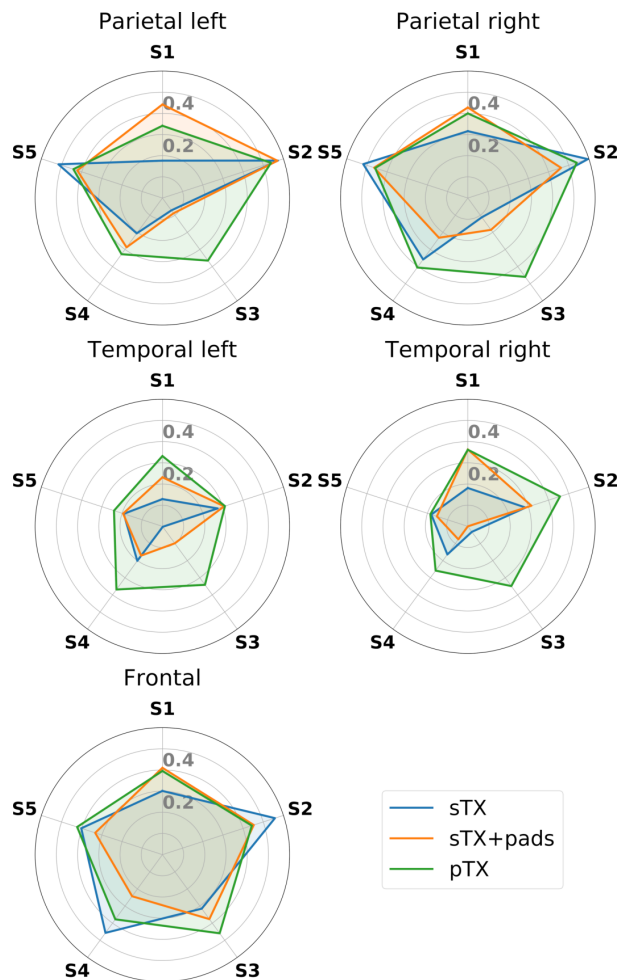


Figure 6: Radar plots of the time-correlation coefficient between the posterior cingulate cortex (seed) and the DMN-associated left parietal, the right parietal, the left temporal, the right temporal and the frontal regions for the five subjects (S1-S5) and the three acquisition modes (sTX, sTX+pads and pTX). Although below significance level due to the small number of subjects involved in this study, this result strongly suggests that higher levels of correlation can be seen in the pTX acquisition mode, in particular in the left and right temporal regions.

480 4. Discussion

481 Parallel transmission has long been advocated as promising technology to
482 tackle standing wave effects at UHF, and enormous progress has been made
483 in the past decade. But to date, the cumbersome operation and need for
484 time-consuming calibrations typically result in these precious resources to be
485 underused in actual application studies. The UP approach circumvents these
486 limitations as it allows for a scanner operation that is no different from a sTX
487 exam. A parallel here can be drawn with another proposed plug and play
488 pTX approach (Cloos et al., 2016), which yet relies on the MR fingerprinting
489 (MRF) concept. The major philosophical difference from UP lies in how the
490 RF field inhomogeneity is dealt with: UPs tackle it at the excitation stage
491 whereas the plug and play MRF technique resolves it at the reconstruction
492 stage by disentangling its effects from the rest of the data. While the latter
493 has shown promising results for quantitative MRI, it is yet not clear how the
494 same framework could be leveraged to fMRI. The UP concept on the other
495 hand is theoretically compatible with any type of MRI acquisition.

496 As shown in a previous work (Gras et al., 2017b), slightly superior pTX
497 excitation performance can be achieved with full subject-specific RF pulse
498 calibrations (Gras et al., 2017b). Another price to pay with UPs is the in-
499 creased SAR and power demands engendered by their broadband behavior to
500 be robust versus the variability of the B_0 offset across subjects (Gras et al.,
501 2017b). The MB-EPI bipolar spoke UPs implemented in this work saturated
502 the peak 10 g SAR of our VOP model (safety factor of 2.3) as well as the
503 peak and total average power constraints, while the MPRAGE and SPACE
504 acquisitions still left a factor of around 2 in TR to manoeuvre with. Consid-

505 ering the integration of pTX into a clinical setting, however, the incremental
506 performance gain of subject-tailored pulses would probably not outweigh the
507 additional effort of calibrating B_1^+ , performing computationally expensive
508 online pulse calculation and other complex pTX-related steps. As an indica-
509 tion of the time that would be needed to perform the calculations (any other
510 operation than the pure pulse optimization taken aside) for this specific pro-
511 tocol in pTX with subject-tailored pulses (slice-specific RF shimming for the
512 MB-EPI sequence and same k_T -point parameterization as for the UPs for
513 the MPRAGE and SPACE sequences), the RF pulse computation times on a
514 DELL Precision 7510 (processor Intel Core i7-6820HQ, 16 Gb of RAM) were
515 10 s, 48 s and 104 s for the MB-EPI, the MPRAGE and the SPACE sequences
516 respectively. These times were returned for 100 iterations of our optimiza-
517 tion algorithm (active-set) and 4 initial random k-space trajectories (for the
518 k_T -points), which is an acceptable trade-off between performance and com-
519 putation time, yet in our experience with low chances to return the global
520 optimum. In addition, the subject-specific approach is prone to errors from
521 any imprecision of the B_1^+ measurement, which is a particular risk in rapid B_1^+
522 mapping (Pohmann et al., 2016). Finally, the subject-specific approach relies
523 on B_0 offset and B_1^+ maps that are typically obtained once at the beginning of
524 the examination, and so any subsequent patient motion will impose further
525 errors. The UP approach effectively removes this risk and provides robust
526 universally applicable dynamic RF shims that are pre-calculated from a set
527 of high-quality calibration data. Interestingly also, the use of UPs provides
528 an additional layer of RF safety in that they can be extensively validated
529 with prior phantom scans (e.g. by temperature mapping). Session-specific

530 subject-tailored RF pulses, as they do not exist until the actual scan occurs,
531 do not allow such extensive RF safety tests and so their compliance with the
532 IEC guidelines can only be assessed by means of numerical SAR simulations
533 (the ones giving rise to the VOP model).

534 In this work, plug and play pTX acquisitions were characterized for the
535 specific example of the HCP-style 7 T whole-brain resting-state fMRI proto-
536 col, by an excitation uniformity of significantly lower CVs than in standard
537 sTX operation without and with dielectric pads. The excitation uniformity
538 of the slice-selective and non-selective UPs that enable plug-and-play pTX
539 were in fact comparable to the B_1^+ uniformity of a volume coil at 3 T, where
540 RF field inhomogeneity in the brain is not considered obstructive to clin-
541 ical use. We furthermore verified experimentally that the improvement in
542 the excitation uniformity translated into a gain in tSNR and in a more ro-
543 bust measurement and analysis of the signal correlations in the resting brain.
544 This is illustrated by the seed-based DMN result (Figure 6) which displayed
545 stronger correlations with the use of pTX UPs than in sTX. One may natu-
546 rally expect that this sensitivity gain translates directly to task-based fMRI.

547 For the MB-EPI acquisition, as shown in 2, we found in flip angle simula-
548 tions that the proposed UP two-spoke design was comparable in performance
549 with the subject-tailored slice-specific RF shimming (one-spoke design) that
550 was recently proposed in HCP-style RS-fMRI scans at 7 T (Wu et al., 2019),
551 and outperformed the subject-tailored volume RF shimming approach. Mov-
552 ing to a one-spoke slice-specific UP on the other hand resulted in significantly
553 impaired excitation quality and robustness across subjects. Here, one subject
554 had a flip angle CV above 16% for the UP RF shimming scenario. As a re-

555 sult, the key advantage of using the UP technique for conducting HCP-style
556 RS-fMRI experiments at 7 T is that it combines the excitation performance
557 typical of subject-tailored slice-specific RF shimming for SMS-EPI with the
558 simplicity of use of sTX. While the first requirement is important to fully
559 exploit the SNR and sensitivity gain at high field, the second is fundamen-
560 tal for the pTX technology to be embraced by new potential users. In the
561 following, we mention some of the limitations that one should be aware of
562 before switching to pTX UPs, and propose directions to mitigate them.

563 Adopting the proposed plug-and-play pTX framework can impose some
564 restrictions on the protocol preparation, in particular for the MB-EPI case.
565 Indeed, for the 2D case, since the two-spoke UP parameters (spokes RF
566 amplitudes and locations in the transmit k-space) are optimized for a fixed
567 slice position, these slice positions, in principle, cannot be modified for the
568 acquisition. To mitigate this, we have proposed a weighted least-squares
569 optimization procedure that promotes some robustness with respect to slice
570 placement. This strategy not only gives a tolerance with respect to the actual
571 position of the slices, but also some tolerance in the slice inclination. As a
572 consequence, it also promotes robustness in terms of flip angle stability in
573 case of motion. Furthermore, by increasing the value of the soft-threshold
574 d_0 (in this study, it was set to 1 cm), it is possible to select a desired degree
575 of robustness, naturally at the expense of performance in the ideal setting.
576 Note here that the MPRAGE and SPACE acquisitions, as well as any 3D
577 sequence, using non-selective dynamic RF shimming pulses, do not have this
578 limitation at all. Hence, for those acquisitions, the position and orientation
579 of the field of view can be set arbitrarily.

580 The fact that the design of UP is dependent of the flip angle that is
581 targeted can appear as another obstacle, in particular if the latter param-
582 eter is supposed to be varied across experiments. We shall note however
583 that the MB-EPI spokes pulses being designed by using the small tip angle
584 approximation, reasonably valid up to 90° (Boulant and Hoult, 2012), dif-
585 ferent flip angles can be targeted by simply scaling the RF waveforms of the
586 pulses. The repetition time of the sequence can be changed as long as the
587 RF power and SAR limits are fulfilled. Just as in sTX acquisitions, the pulse
588 duration likewise can be adjusted to accommodate these constraints, with-
589 out having to recalculate the pulses, yet with increased penalty with respect
590 to B_0 robustness. To provide more optimal solutions, different sets of pulses
591 with different energy loads but identical duration could also be designed. The
592 small tip angle and refocusing pulses in the MPRAGE and SPACE sequences
593 being scalable as well, the same reasoning holds for the 3D anatomical scans.

594 The fact that the UP framework requires the adoption of bipolar 2-spoke
595 pulses to preserve the same quality of excitation as the subject-tailored slice-
596 specific RF shim does not impose a significant penalty in terms of the time-
597 efficiency of the pulse, since the only excitation time overhead amounts to
598 twice the ramp duration of the slice selection gradient. However, a limitation
599 of the current implementation, and which does not exist for 1-spoke pulses, is
600 that the slices could not be tilted (although this functionality can be desirable
601 in practice, e.g. to maximize brain coverage with a minimum number of
602 slices). This limitation is due to the way the gradient delay correction was
603 performed, namely the application of a slice-dependent RF phase offset to
604 the second spoke RF pulse (Gras et al., 2017c). This strategy unfortunately

605 does not allow slice tilting unless the gradient delay is the same for the x ,
606 y and z gradient coils. This however can be overcome in future work by
607 adopting a more general correction strategy which consists in encoding the
608 gradient delay correction in the second spoke k-space location rather than in
609 the second spoke RF phase, by using so-called trim-blips (Oelhafen et al.,
610 2004).

611 **Conclusions**

612 Calibration-free pTX was successfully implemented in the entire HCP RS-
613 fMRI protocol at 7 T, including anatomical scans, by means of slice-specific
614 bipolar two-spoke SMS-UPs (MB=5) and non-selective k_T point UPs. The
615 flip angle homogeneity reported in this study with universal slice-specific
616 two-spoke MB-EPI pulses (9 to 11% across 5 subjects) is comparable to
617 the flip angle homogeneity obtained with subject-tailored slice-specific RF
618 shim pulses. With this work, we report for the first time a plug and play
619 utilization of a multi-transmit multi-receive RF coil for whole-brain BOLD
620 fMRI at ultra-high field which, for MB-EPI, gives access to the same quality
621 of excitation as subject-tailored slice-specific RF shimming without deviating
622 from simple routine scanning. As compared with the single transmission
623 mode, with and without dielectric pads, a noticeable gain in tSNR (up to 2-
624 fold in B_1^+ deprived regions) resulting into a higher sensitivity for the BOLD-
625 induced neural activity, and an improved contrast uniformity in whole-brain
626 anatomical scans were reported.

627 **Acknowledgements**

628 The research leading to these results has received funding from the Euro-
629 pean Research Council under the European Unions Seventh Framework Pro-
630 gram (FP7/2013-2018), ERC Grant Agreement n. 309674. BAP is funded by
631 the Netherlands Organization for Scientific Research (NWO 016.Vidi.178.052)
632 and the National Institute of Health (R01MH111444, PI Feinberg). XW is
633 supported by grants from National Institute of Health (U01 EB025144 and
634 P41 EB015894, PI Ugurbil). The authors wish to thank Bertrand Thirion
635 and Florent Meyniel for valuable discussions regarding the resting-state fMRI
636 analysis, Alexandre Vignaud for valuable discussions on dielectric padding,
637 Franck Mauconduit for his contribution to the MPRAGE and SPACE se-
638 quences and for setting up the B_1^+ calibration protocol, and Desmond Tse
639 for his contributions to the pTX MB-EPI sequence. Data were acquired at
640 Scannexus BV in Maastricht, The Netherlands.

641 **Competing interests**

642 CEA has filed provisional patent applications directed to this technology.

643 **References**

644 A. Abraham, F. Pedregosa, M. Eickenberg, P. Gervais, A. Mueller, J. Kos-
645 saifi, A. Gramfort, B. Thirion, and G. Varoquaux. Machine learning for
646 neuroimaging with scikit-learn. *Frontiers in Neuroinformatics*, 8, 2014.
647 ISSN 1662-5196. doi: 10.3389/fninf.2014.00014. URL [http://journal.
648 frontiersin.org/article/10.3389/fninf.2014.00014/abstract](http://journal.frontiersin.org/article/10.3389/fninf.2014.00014/abstract).

- 649 J. L. Andersson, S. Skare, and J. Ashburner. How to correct suscep-
650 tibility distortions in spin-echo echo-planar images: application to dif-
651 fusion tensor imaging. *NeuroImage*, 20(2):870–888, Oct. 2003. ISSN
652 10538119. doi: 10.1016/S1053-8119(03)00336-7. URL [http://linkinghub.
653 elsevier.com/retrieve/pii/S1053811903003367](http://linkinghub.elsevier.com/retrieve/pii/S1053811903003367).
- 654 Y. Behzadi, K. Restom, J. Liau, and T. T. Liu. A component based noise
655 correction method (CompCor) for BOLD and perfusion based fMRI. *Neu-
656 roimage*, 37(1):90–101, 2007.
- 657 A. Beqiri, H. Hoogduin, A. Sbrizzi, J. V. Hajnal, and S. J. Malik. Whole-
658 brain 3D FLAIR at 7T using direct signal control. *Magnetic Resonance
659 in Medicine*, 0(0), 2018. ISSN 1522-2594. doi: 10.1002/mrm.27149. URL
660 <https://onlinelibrary.wiley.com/doi/abs/10.1002/mrm.27149>.
- 661 N. Boulant and D. I. Hoult. High tip angle approximation based on a modi-
662 fied BlochRiccati equation. *Magn Reson Med*, 67(2):339–343, 2012. ISSN
663 1522-2594. doi: 10.1002/mrm.23270. URL [http://dx.doi.org/10.1002/
664 mrm.23270](http://dx.doi.org/10.1002/mrm.23270).
- 665 N. Boulant, D. Le Bihan, and A. Amadon. Strongly modulating pulses: a new
666 method for tackling RF inhomogeneity problems at high fields. *Magnetic
667 Resonance in Medicine*, 68:701–708, 2008.
- 668 N. Boulant, V. Gras, A. Amadon, G. Ferrand, and A. Vignaud. Workflow
669 proposal for defining SAR safety margins in parallel transmission. In *Pro-
670 ceedings of the 26th Annual Meeting of ISMRM*, page Abstract 295, Paris,
671 2018.

- 672 D. O. Brunner and K. P. Pruessmann. B1+ interferometry for the calibra-
673 tion of RF transmitter arrays. *Magn Reson Med*, 61(6):1480–1488, 2009.
674 ISSN 1522-2594. doi: 10.1002/mrm.21893. URL [http://dx.doi.org/10.
675 1002/mrm.21893](http://dx.doi.org/10.1002/mrm.21893).
- 676 S. F. Cauley, J. R. Polimeni, H. Bhat, L. L. Wald, and K. Setsompop. Inter-
677 slice leakage artifact reduction technique for simultaneous multislice ac-
678 quisitions. *Magnetic Resonance in Medicine*, 72(1):93–102, July 2014.
679 ISSN 1522-2594. doi: 10.1002/mrm.24898. URL [https://onlinelibrary.
680 wiley.com/doi/abs/10.1002/mrm.24898](https://onlinelibrary.wiley.com/doi/abs/10.1002/mrm.24898).
- 681 M. A. Cloos, N. Boulant, M. Luong, G. Ferrand, E. Giacomini, M.-F. Hang,
682 C. J. Wiggins, D. L. Bihan, and A. Amadon. Parallel-transmission-enabled
683 magnetization-prepared rapid gradient-echo T1-weighted imaging of the
684 human brain at 7T. *NeuroImage*, 62(3):2140–2150, 2012a. ISSN 1053-
685 8119. doi: <http://dx.doi.org/10.1016/j.neuroimage.2012.05.068>. URL
686 <http://www.sciencedirect.com/science/article/pii/S1053811912005563>.
- 687 M. A. Cloos, N. Boulant, M. Luong, G. Ferrand, E. Giacomini, D. Le Bihan,
688 and A. Amadon. kT-points: Short three-dimensional tailored RF pulses
689 for flip-angle homogenization over an extended volume. *Magn Reson Med*,
690 67(1):72–80, 2012b. ISSN 1522-2594. doi: 10.1002/mrm.22978. URL
691 <http://dx.doi.org/10.1002/mrm.22978>.
- 692 M. A. Cloos, F. Knoll, T. Zhao, K. T. Block, M. Bruno, G. C. Wiggins,
693 and D. K. Sodickson. Multiparametric imaging with heterogeneous ra-
694 diofrequency fields. *Nature Communications*, 7:12445, Aug. 2016. ISSN

695 2041-1723. doi: 10.1038/ncomms12445. URL [https://www.nature.com/
696 articles/ncomms12445](https://www.nature.com/articles/ncomms12445).

697 L. Dupas, A. Massire, A. Amadon, A. Vignaud, and N. Boulant. Two-
698 spoke placement optimization under explicit specific absorption rate and
699 power constraints in parallel transmission at ultra-high field. *Journal of
700 Magnetic Resonance*, 255(0):59–67, 2015. ISSN 1090-7807. doi: [http:
701 //dx.doi.org/10.1016/j.jmr.2015.03.013](http://dx.doi.org/10.1016/j.jmr.2015.03.013). URL [http://www.sciencedirect.
702 com/science/article/pii/S1090780715000750](http://www.sciencedirect.com/science/article/pii/S1090780715000750).

703 F. Eggenschwiler, K. R. O’Brien, R. Gruetter, and J. P. Marques. Improving
704 T2-weighted imaging at high field through the use of kT-points. *Magnetic
705 Resonance in Medicine*, 71(4):1478–1488, 2014. ISSN 1522-2594. doi: 10.
706 1002/mrm.24805. URL <http://dx.doi.org/10.1002/mrm.24805>.

707 G. Eichfelder and M. Gebhardt. Local specific absorption rate control for
708 parallel transmission by virtual observation points. *Magn Reson Med*, 66
709 (5):1468–1476, 2011. ISSN 1522-2594. doi: 10.1002/mrm.22927. URL
710 <http://dx.doi.org/10.1002/mrm.22927>.

711 H.-P. Fautz, M. Vogel, P. Gross, A. Kerr, and Y. Zhu. B1 mapping of coil
712 arrays for parallel transmission. In *Proceedings of the 16th Annual Meeting
713 of ISMRM*, page 1247, 2008.

714 M. Garrec, V. Gras, M.-F. Hang, G. Ferrand, M. Luong, and N. Boulant.
715 Probabilistic analysis of the specific absorption rate intersubject vari-
716 ability safety factor in parallel transmission MRI. *Magnetic Resonance*

- 717 *in Medicine*, 78(3):1217–1223, 2016. doi: 10.1002/mrm.26468. URL
718 <https://onlinelibrary.wiley.com/doi/abs/10.1002/mrm.26468>.
- 719 M. F. Glasser, S. N. Sotiropoulos, J. A. Wilson, T. S. Coalson, B. Fischl,
720 J. L. Andersson, J. Xu, S. Jbabdi, M. Webster, J. R. Polimeni, D. C. V.
721 Essen, and M. Jenkinson. The minimal preprocessing pipelines for the
722 Human Connectome Project. *NeuroImage*, 80:105 – 124, 2013. ISSN 1053-
723 8119. doi: <https://doi.org/10.1016/j.neuroimage.2013.04.127>. URL <http://www.sciencedirect.com/science/article/pii/S1053811913005053>. Map-
724 ping the Connectome.
725
- 726 G. Goelman, R. Dan, F. Rika, O. Bezdicek, E. Rika, J. Roth, J. Vymazal,
727 and R. Jech. Frequency-phase analysis of resting-state functional MRI.
728 *Scientific Reports*, 7:43743, Mar. 2017. ISSN 2045-2322. doi: 10.1038/
729 [srep43743](http://www.nature.com/articles/srep43743). URL <http://www.nature.com/articles/srep43743>.
- 730 V. Gras, A. Vignaud, F. Mauconduit, M. Luong, A. Amadon, D. Le Bi-
731 han, and N. Boulant. Signal-domain optimization metrics for MPRAGE
732 RF pulse design in parallel transmission at 7 tesla: Signal-Domain Opti-
733 mization Metrics for MPRAGE RF Pulse Design. *Magnetic Resonance in*
734 *Medicine*, 76:1431–1442, 2016. ISSN 07403194. doi: 10.1002/mrm.26043.
735 URL <http://doi.wiley.com/10.1002/mrm.26043>.
- 736 V. Gras, M. Boland, A. Vignaud, G. Ferrand, A. Amadon, F. Maucon-
737 duit, D. L. Bihan, T. Stöcker, and N. Boulant. Homogeneous non-
738 selective and slice-selective parallel-transmit excitations at 7 Tesla with
739 universal pulses: A validation study on two commercial RF coils. *PLOS*
740 *ONE*, 12(8):e0183562, 2017a. ISSN 1932-6203. doi: 10.1371/journal.

741 pone.0183562. URL <http://journals.plos.org/plosone/article?id=10.1371/>
742 [journal.pone.0183562](http://journals.plos.org/plosone/article?id=10.1371/journal.pone.0183562).

743 V. Gras, A. Vignaud, A. Amadon, D. Le Bihan, and N. Boulant. Universal
744 pulses: A new concept for calibration-free parallel transmission. *Magnetic*
745 *Resonance in Medicine*, 77:635–643, 2017b. ISSN 1522-2594. doi: 10.1002/
746 [mrm.26148](http://dx.doi.org/10.1002/mrm.26148). URL <http://dx.doi.org/10.1002/mrm.26148>.

747 V. Gras, A. Vignaud, A. Amadon, F. Mauconduit, D. Le Bihan, and
748 N. Boulant. New method to characterize and correct with sub-s pre-
749 cision gradient delays in bipolar multispoke RF pulses. *Magnetic Res-*
750 *onance in Medicine*, 78:2194–2202, Jan. 2017c. ISSN 1522-2594. doi:
751 [10.1002/mrm.26614](http://dx.doi.org/10.1002/mrm.26614). URL [http://onlinelibrary.wiley.com/doi/10.1002/](http://onlinelibrary.wiley.com/doi/10.1002/mrm.26614/abstract)
752 [mrm.26614/abstract](http://onlinelibrary.wiley.com/doi/10.1002/mrm.26614/abstract).

753 V. Gras, F. Mauconduit, A. Vignaud, A. Amadon, D. Le Bihan, T. Stöcker,
754 and N. Boulant. Design of universal parallel-transmit refocusing k_t -point
755 pulses and application to 3D T_2 -weighted imaging at 7T: Universal Pulse
756 Design of 3d Refocusing Pulses. *Magnetic Resonance in Medicine*, 80(1):
757 53–65, July 2018. ISSN 07403194. doi: 10.1002/mrm.27001. URL [http://](http://doi.wiley.com/10.1002/mrm.27001)
758 doi.wiley.com/10.1002/mrm.27001.

759 W. Grissom, C.-y. Yip, Z. Zhang, V. A. Stenger, J. A. Fessler, and D. C. Noll.
760 Spatial domain method for the design of RF pulses in multicoil parallel
761 excitation. *Magn Reson Med*, 56(3):620–629, 2006. ISSN 1522-2594. doi:
762 [10.1002/mrm.20978](http://dx.doi.org/10.1002/mrm.20978). URL <http://dx.doi.org/10.1002/mrm.20978>.

763 M. A. Griswold, P. M. Jakob, R. M. Heidemann, M. Nittka, V. Jellus,

- 764 J. Wang, B. Kiefer, and A. Haase. Generalized autocalibrating partially
765 parallel acquisitions (GRAPPA). *Magnetic Resonance in Medicine*, 47(6):
766 1202–1210, June 2002. ISSN 0740-3194, 1522-2594. doi: 10.1002/mrm.
767 10171. URL <http://doi.wiley.com/10.1002/mrm.10171>.
- 768 R. Gumbrecht. *Development of customized pTx MR excitation methods*
769 *and their safe application*. PhD thesis, Friedrich-Alexander-Universität
770 Erlangen-Nürnberg, Erlangen, Oct. 2013.
- 771 A. Hoyos-Idrobo, P. Weiss, A. Massire, A. Amadon, and N. Boulant. On
772 Variant Strategies to Solve the Magnitude Least Squares Optimization
773 Problem in Parallel Transmission Pulse Design and Under Strict SAR and
774 Power Constraints. *IEEE Transactions on Medical Imaging*, 33(3):739–
775 748, Mar. 2014. ISSN 0278-0062. doi: 10.1109/TMI.2013.2295465.
- 776 International Electrotechnical Commission. *IEC 60601-2-33 Medical Electric*
777 *Equipment - Part 2-33: Particular Requirements for the Basic Safety*
778 *and Essential Performance*. 3.2 edition, 2015. ISBN 978-2-8322-2743-5.
- 779 M. Jenkinson and S. Smith. A global optimisation method for robust affine
780 registration of brain images. *Medical Image Analysis*, 5(2):143–156, June
781 2001. ISSN 1361-8415. doi: 10.1016/S1361-8415(01)00036-6. URL <http://www.sciencedirect.com/science/article/pii/S1361841501000366>.
- 783 M. Jenkinson, P. Bannister, M. Brady, and S. Smith. Improved Optimiza-
784 tion for the Robust and Accurate Linear Registration and Motion Cor-
785 rection of Brain Images. *NeuroImage*, 17(2):825–841, Oct. 2002. ISSN

786 10538119. doi: 10.1006/nimg.2002.1132. URL <http://linkinghub.elsevier.com/retrieve/pii/S1053811902911328>.

788 U. Katscher, P. Börnert, C. Leussler, and J. S. van den Brink. Transmit
789 SENSE. *Magn Reson Med*, 49(1):144–150, 2003. ISSN 1522-2594. doi:
790 10.1002/mrm.10353. URL <http://dx.doi.org/10.1002/mrm.10353>.

791 N. Krishnamurthy, T. Santini, S. Wood, J. Kim, T. Zhao, H. J. Aizenstein,
792 and T. S. Ibrahim. Computational and experimental evaluation of the
793 Tic-Tac-Toe RF coil for 7 Tesla MRI. *PLOS ONE*, 14(1):e0209663, Jan.
794 2019. ISSN 1932-6203. doi: 10.1371/journal.pone.0209663. URL <https://journals.plos.org/plosone/article?id=10.1371/journal.pone.0209663>.

796 A. Massire, A. Vignaud, B. Robert, D. Le Bihan, N. Boulant, and
797 A. Amadon. Parallel-transmission-enabled three-dimensional T2-weighted
798 imaging of the human brain at 7 Tesla. *Magnetic Resonance in Medicine*,
799 73:2195–2203, 2015. ISSN 1522-2594. doi: 10.1002/mrm.25353. URL
800 <http://dx.doi.org/10.1002/mrm.25353>.

801 S. Moeller, E. Yacoub, C. A. Olman, E. Auerbach, J. Strupp, N. Harel,
802 and K. Uğurbil. Multiband multislice GE-EPI at 7 tesla, with 16-fold
803 acceleration using partial parallel imaging with application to high spatial
804 and temporal whole-brain fMRI. *Magnetic Resonance in Medicine*, 63(5):
805 1144–1153, May 2010. ISSN 1522-2594. doi: 10.1002/mrm.22361. URL
806 <http://onlinelibrary.wiley.com/doi/10.1002/mrm.22361/abstract>.

807 J. P. Mugler. Optimized three-dimensional fast-spin-echo MRI. *J. Magn.*
808 *Reson. Imaging*, 39(4):745–767, Apr. 2014. ISSN 1522-2586. doi: 10.1002/

809 jmri.24542. URL <http://onlinelibrary.wiley.com/doi/10.1002/jmri.24542/>
810 abstract.

811 J. P. Mugler and J. R. Brookeman. Three-dimensional magnetization-
812 prepared rapid gradient-echo imaging (3d MP RAGE). *Magn Reson Med*,
813 15:152–157, 1990.

814 J. P. Mugler, B. Kiefer, and J. R. Brookeman. Three-dimensional T2-
815 weighted imaging of the brain using very long spin-echo trains. In *Pro-*
816 *ceedings of the 8th Annual Meeting of ISMRM*, page 687, 2000.

817 M. Oelhafen, K. P. Pruessmann, S. Kozerke, and P. Boesiger. Calibration
818 of echo-planar 2D-selective RF excitation pulses. *Magnetic Resonance in*
819 *Medicine*, 52(5):1136–1145, Nov. 2004. ISSN 0740-3194, 1522-2594. doi:
820 10.1002/mrm.20248. URL <http://doi.wiley.com/10.1002/mrm.20248>.

821 F. Padormo, A. Beqiri, J. V. Hajnal, and S. J. Malik. Parallel transmission
822 for ultrahighfield imaging. *NMR Biomed*, 29(9):1145–1161, Sept. 2016.
823 ISSN 0952-3480. doi: 10.1002/nbm.3313. URL [https://www.ncbi.nlm.nih.](https://www.ncbi.nlm.nih.gov/pmc/articles/PMC4995736/)
824 [gov/pmc/articles/PMC4995736/](https://www.ncbi.nlm.nih.gov/pmc/articles/PMC4995736/).

825 J. Pauly, D. Nishimura, and A. Macovski. A k-space analysis of
826 small-tip-angle excitation. *Journal of Magnetic Resonance*, 81(1):
827 43 – 56, 1989a. ISSN 0022-2364. doi: [http://dx.doi.org/10.](http://dx.doi.org/10.1016/0022-2364(89)90265-5)
828 [1016/0022-2364\(89\)90265-5](http://dx.doi.org/10.1016/0022-2364(89)90265-5). URL [http://www.sciencedirect.com/science/](http://www.sciencedirect.com/science/article/pii/0022236489902655)
829 [article/pii/0022236489902655](http://www.sciencedirect.com/science/article/pii/0022236489902655).

830 J. Pauly, D. Nishimura, and A. Macovski. A linear class of large-tip-
831 angle selective excitation pulses. *Journal of Magnetic Resonance*, 82

832 (3):571 – 587, 1989b. ISSN 0022-2364. doi: [http://dx.doi.org/10.1016/0022-2364\(89\)90219-9](http://dx.doi.org/10.1016/0022-2364(89)90219-9). URL <http://www.sciencedirect.com/science/article/pii/0022236489902199>.

835 R. Pohmann, O. Speck, and K. Scheffler. Signal-to-noise ratio and MR tissue
836 parameters in human brain imaging at 3, 7, and 9.4 tesla using current
837 receive coil arrays. *Magnetic Resonance in Medicine*, 75(2):801–809, 2016.
838 ISSN 1522-2594. doi: 10.1002/mrm.25677. URL <http://dx.doi.org/10.1002/mrm.25677>.

840 J. R. Polimeni, H. Bhat, T. Witzel, T. Benner, T. Feiweier, S. J. Inati,
841 V. Renvall, K. Heberlein, and L. L. Wald. Reducing sensitivity losses due to
842 respiration and motion in accelerated Echo Planar Imaging by reordering
843 the auto-calibration data acquisition. *Magn Reson Med*, 75(2):665–679,
844 Feb. 2016. ISSN 0740-3194. doi: 10.1002/mrm.25628. URL <https://www.ncbi.nlm.nih.gov/pmc/articles/PMC4580494/>.

846 M. E. Raichle, A. M. MacLeod, A. Z. Snyder, W. J. Powers, D. A. Gusnard,
847 and G. L. Shulman. A default mode of brain function. *Proceedings of the*
848 *National Academy of Sciences*, 98(2):676–682, 2001.

849 S. Saekho, C.-y. Yip, D. C. Noll, F. E. Boada, and V. A. Stenger. Fast-kz
850 three-dimensional tailored radiofrequency pulse for reduced B1 inhomogeneity.
851 *Magnetic Resonance in Medicine*, 55(4):719–724, 2006. ISSN
852 1522-2594. doi: 10.1002/mrm.20840. URL <http://dx.doi.org/10.1002/mrm.20840>.

854 K. Setsompop, V. Alagappan, B. Gagoski, T. Witzel, J. Polimeni, A. Pot-

855 thast, F. Hebrank, U. Fontius, F. Schmitt, L. L. Wald, and E. Adalsteins-
856 son. Slice-selective RF pulses for in vivo B1+ inhomogeneity mitigation
857 at 7 tesla using parallel RF excitation with a 16-element coil. *Magnetic*
858 *Resonance in Medicine*, 60(6):1422–1432, 2008. ISSN 1522-2594. doi:
859 10.1002/mrm.21739. URL <http://dx.doi.org/10.1002/mrm.21739>.

860 K. Setsompop, B. A. Gagoski, J. R. Polimeni, T. Witzel, V. J. Wedeen,
861 and L. L. Wald. Blipped-controlled aliasing in parallel imaging for si-
862 multaneous multislice echo planar imaging with reduced g-factor penalty.
863 *Magnetic Resonance in Medicine*, 67(5):1210–1224, May 2012. ISSN 1522-
864 2594. doi: 10.1002/mrm.23097. URL [https://onlinelibrary.wiley.com/doi/](https://onlinelibrary.wiley.com/doi/abs/10.1002/mrm.23097)
865 [abs/10.1002/mrm.23097](https://onlinelibrary.wiley.com/doi/abs/10.1002/mrm.23097).

866 S. M. Smith, P. T. Fox, K. L. Miller, D. C. Glahn, P. M. Fox, C. E. Mackay,
867 N. Filippini, K. E. Watkins, R. Toro, A. R. Laird, and C. F. Beckmann.
868 Correspondence of the brain’s functional architecture during activation
869 and rest. *Proceedings of the National Academy of Sciences of the United*
870 *States of America*, 106(31):13040–13045, Aug. 2009. ISSN 0027-8424.
871 doi: 10.1073/pnas.0905267106. URL [https://www.ncbi.nlm.nih.gov/pmc/](https://www.ncbi.nlm.nih.gov/pmc/articles/PMC2722273/)
872 [articles/PMC2722273/](https://www.ncbi.nlm.nih.gov/pmc/articles/PMC2722273/).

873 D. H. Tse, C. J. Wiggins, and B. A. Poser. Estimating and eliminating
874 the excitation errors in bipolar gradient composite excitations caused by
875 radiofrequency-gradient delay: Example of bipolar spokes pulses in parallel
876 transmission. *Magnetic Resonance in Medicine*, 78(5):1883–1890, 2016.
877 doi: 10.1002/mrm.26586. URL [https://onlinelibrary.wiley.com/doi/abs/](https://onlinelibrary.wiley.com/doi/abs/10.1002/mrm.26586)
878 [10.1002/mrm.26586](https://onlinelibrary.wiley.com/doi/abs/10.1002/mrm.26586).

879 K. Uğurbil, J. Xu, E. J. Auerbach, S. Moeller, A. T. Vu, J. M. Duarte-
880 Carvajalino, C. Lenglet, X. Wu, S. Schmitter, P. F. V. de Moorlele,
881 J. Strupp, G. Sapiro, F. D. Martino, D. Wang, N. Harel, M. Garwood,
882 L. Chen, D. A. Feinberg, S. M. Smith, K. L. Miller, S. N. Sotiropou-
883 los, S. Jbabdi, J. L. Andersson, T. E. Behrens, M. F. Glasser, D. C. V.
884 Essen, and E. Yacoub. Pushing spatial and temporal resolution for func-
885 tional and diffusion MRI in the Human Connectome Project. *NeuroIm-*
886 *age*, 80:80 – 104, 2013. ISSN 1053-8119. doi: [https://doi.org/10.1016/](https://doi.org/10.1016/j.neuroimage.2013.05.012)
887 [j.neuroimage.2013.05.012](https://doi.org/10.1016/j.neuroimage.2013.05.012). URL [http://www.sciencedirect.com/science/](http://www.sciencedirect.com/science/article/pii/S1053811913005065)
888 [article/pii/S1053811913005065](http://www.sciencedirect.com/science/article/pii/S1053811913005065). Mapping the Connectome.

889 D. C. Van Essen, S. M. Smith, D. M. Barch, T. E. J. Behrens, E. Ya-
890 coub, and K. Uğurbil. The WU-Minn Human Connectome Project: An
891 overview. *NeuroImage*, 80:62–79, Oct. 2013. ISSN 1053-8119. doi:
892 [10.1016/j.neuroimage.2013.05.041](https://doi.org/10.1016/j.neuroimage.2013.05.041). URL [http://www.sciencedirect.com/](http://www.sciencedirect.com/science/article/pii/S1053811913005351)
893 [science/article/pii/S1053811913005351](http://www.sciencedirect.com/science/article/pii/S1053811913005351).

894 J. L. Vincent, A. Z. Snyder, M. D. Fox, B. J. Shannon, J. R. Andrews, M. E.
895 Raichle, and R. L. Buckner. Coherent Spontaneous Activity Identifies a
896 Hippocampal-Parietal Memory Network. *Journal of Neurophysiology*, 96
897 (6):3517–3531, Dec. 2006. ISSN 0022-3077, 1522-1598. doi: [10.1152/jn.](https://doi.org/10.1152/jn.00048.2006)
898 [00048.2006](https://doi.org/10.1152/jn.00048.2006). URL <http://www.physiology.org/doi/10.1152/jn.00048.2006>.

899 A. T. Vu, K. Jamison, M. F. Glasser, S. M. Smith, T. Coalson, S. Moeller,
900 E. J. Auerbach, K. Uğurbil, and E. Yacoub. Tradeoffs in pushing the
901 spatial resolution of fMRI for the 7T Human Connectome Project. *Neu-*
902 *roImage*, 154:23 – 32, 2017. ISSN 1053-8119. doi: <https://doi.org/>

903 10.1016/j.neuroimage.2016.11.049. URL <http://www.sciencedirect.com/science/article/pii/S1053811916306681>. Cleaning up the fMRI time series:
904 Mitigating noise with advanced acquisition and correction strategies.
905

906 A. Webb. Dielectric materials in magnetic resonance. *Concepts in Magnetic
907 Resonance Part A*, 38A(4):148–184, July 2011. ISSN 15466086. doi: 10.
908 1002/cmr.a.20219. URL <http://doi.wiley.com/10.1002/cmr.a.20219>.

909 E. Wong. Optimized phase schedules for minimizing peak RF power in si-
910 multaneous multi-slice RF excitation pulses. *In Proceedings of the 20th
911 Annual Meeting of ISMRM*, page 2209, 2012.

912 X. Wu, S. Schmitter, E. J. Auerbach, S. Moeller, K. Uğurbil, and P.-F.
913 Van de Moortele. Simultaneous multislice multiband parallel radiofre-
914 quency excitation with independent slice-specific transmit B1 homoge-
915 nization: Simultaneous Multislice Parallel RF Excitation. *Magnetic Res-
916 onance in Medicine*, 70(3):630–638, Sept. 2013. ISSN 07403194. doi:
917 10.1002/mrm.24828. URL <http://doi.wiley.com/10.1002/mrm.24828>.

918 X. Wu, E. J. Auerbach, A. T. Vu, S. Moeller, C. Lenglet, S. Schmitter, P.-F.
919 Van de Moortele, E. Yacoub, and K. Uğurbil. High-resolution whole-brain
920 diffusion mri at 7T using radiofrequency parallel transmission. *Magnetic
921 Resonance in Medicine*, 80(5):1857–1870, 2018. doi: 10.1002/mrm.27189.
922 URL <https://onlinelibrary.wiley.com/doi/abs/10.1002/mrm.27189>.

923 X. Wu, E. J. Auerbach, A. T. Vu, S. Moeller, P.-F. Van de Moortele,
924 E. Yacoub, and K. Uğurbil. Human Connectome Project-style resting-
925 state functional MRI at 7 Tesla using radiofrequency parallel transmis-

926 sion. *NeuroImage*, 184:396–408, Jan. 2019. ISSN 1053-8119. doi:
927 10.1016/j.neuroimage.2018.09.038. URL [http://www.sciencedirect.com/
928 science/article/pii/S1053811918308231](http://www.sciencedirect.com/science/article/pii/S1053811918308231).

929 E. Yacoub, A. Shmuel, J. Pfeuffer, P.-F. Van De Moortele, G. Adriany, P. An-
930 dersen, J. T. Vaughan, H. Merkle, K. Uğurbil, and X. Hu. Imaging brain
931 function in humans at 7 Tesla. *Magnetic Resonance in Medicine*, 45(4):
932 588–594, Mar. 2001. ISSN 0740-3194. doi: 10.1002/mrm.1080. URL
933 <https://onlinelibrary.wiley.com/doi/abs/10.1002/mrm.1080>.

934 Y. Zhu. Parallel excitation with an array of transmit coils. *Magnetic Reso-*
935 *nance in Medicine*, 51(4):775–784, 2004. URL [http://onlinelibrary.wiley.
936 com/doi/10.1002/mrm.20011/full](http://onlinelibrary.wiley.com/doi/10.1002/mrm.20011/full).